Surface & Coatings Technology 452 (2023) 129107

Contents lists available at ScienceDirect

Surface & Coatings Technology

journal homepage: www.elsevier.com/locate/surfcoat

Polymer infiltration synthesis of inorganic nanoporous coatings: Does polymer template affect their properties?

Khalil Omotosho [a], John Tran [a], Elena V. Shevchenko [b,c,**], Diana Berman [a,*]

[a] Materials Science and Engineering Department, University of North Texas, 1155 Union Circle, Denton, TX 76203, USA
[b] Center for Nanoscale Materials, Argonne National Laboratory, Argonne, IL 60439, USA
[c] Department of Chemistry and James Franck Institute, University of Chicago, Chicago, IL 60637, USA

ARTICLE INFO

Keywords:
Nanoporous coatings
Zinc oxide
Polymer infiltration synthesis
Sensing

ABSTRACT

Synthesis of all-inorganic metal oxide architectures using polymer templates offers control over their thickness, porosity, and composition. Here, we provide insights into the synthesis of nanoporous zinc oxide films as a model system via infiltration of polymers that have different mechanisms of interaction with metal oxide precursors such as a polymer of intrinsic microporosity (PIM-1) and representative of the *block*-copolymers family (polystyrene-polyvinyl pyridine block copolymer). We investigated polymer infiltration process with both gas (diethyl zinc, DEZ, and water vapors) and solution (zinc acetylacetonate, $Zn(acac)_2$, dissolved in ethanol) phase precursors. Using quartz crystal microbalance (QCM), X-ray diffraction (XRD), and X-ray photoelectron spectroscopy (XPS) analyses, we systematically studied the effect of polymer template and the form of the metal oxide precursors on the properties of synthesized metal oxide thin coatings. We demonstrate that the infiltration of polymer templates can be efficiently achieved using both gas phase and solution phase precursors. We show that the crystallinity of the synthesized 200 nm ZnO films is mainly affected by the state of the precursor (gas or solution phase) and does not depend on the polymer template type. In turn, the polymer type affects the surface termination of ZnO films. We demonstrate that the surface of porous ZnO coatings synthesized with BCP (here PS-P4VP) is more accessible than the surface of ZnO synthesized with PIM; however, despite the lower surface accessibility for ethanol molecules, ZnO synthesized via infiltration of PIM-1 with solution-phase precursors demonstrates the largest change in resistivity upon its exposure to ethanol vapor at room temperature.

1. Introduction

Template-assisted infiltration synthesis has been efficiently used for creating composite [1–8] and all-inorganic porous metal [9,10] and metal oxide structures [9]. Organic polymers can be exposed to gas phase metalorganic precursors [11] (so-called sequential infiltration synthesis (SIS) or vapor phase infiltration (VPI)) [9,12,13] or metal ions dissolved in solution [10,14–17] to transform them into hybrid materials. Polymer templates can be further removed via thermal oxidative annealing [10,18] or plasma treatment [19] resulting in the synthesis of all-inorganic metal oxides architectures with features resembling the structure of the polymer. All polymers with functional groups capable of interacting with gas or solution phase metal precursors can be used to synthesize hybrid or all-inorganic structures for a broad range of applications [20,21] such as solvent separation membranes [22], reusable absorbers for oil spill mitigation [8], sensors [23,24] and antireflective coatings [18].

Various polymer templates such as block copolymers (BCPs) consisting of polar and nonpolar domains (e.g. polystyrene-*block*-polyvinyl pyridine (PS-b-P4VP) [23,25], PS-b-P2VP [24], polystyrene-*block*-polymethylmethacrylate (PS-b-PMMA) [26,27], *etc*), polymers that carry polar groups (e.g. UV-curable photoresists SU-8 [28–29] or polymethylmethacrylate [30]), hydrogels [10] and polymers of intrinsic microporosity (PIM) [22,31,32] have been utilized as templates in SIS [9,11,20]. The use of BCPs and PIM as templates allows to engineer porous hybrids that can further transform into porous all-inorganic structures after polymer removal [9]. However, the mechanism of interactions of BCPs and PIMs with gas-phase precursors seems to be different. In the case of BCP, the gas phase precursors (e.g. trimethylaluminum (TMA)) interact with polar groups (e.g. carbonyl groups) of the

* Correspondence to: E. Shevchenko, Center for Nanoscale Materials, Argonne National Laboratory, Argonne, IL 60439, USA.
** Corresponding author.
E-mail addresses: eshevchenko@anl.gov (E.V. Shevchenko), diana.berman@unt.edu (D. Berman).

https://doi.org/10.1016/j.surfcoat.2022.129107
Received 14 September 2022; Received in revised form 3 November 2022; Accepted 23 November 2022
Available online 29 November 2022

hydrophilic part of the BCP, forming physisorbed complexes and covalently bonded products [33]. In turn, PIMs have porous structure with a pore size less than 2 nm, originating from rigid backbones which inhibit efficient molecular chain packing [34,35]. In the case of PIMs, metal precursors interact with functional groups of PIMs (e.g. C≡N groups) forming an adduct that transforms into hydroxide upon its exposure to H_2O that detaches from the polymer and further serves as a nucleation center for growth of oxide phase [22]. The same gas or solution phase metal oxide precursors and synthesis regimes can be used for the synthesis of porous metal oxides using BCPs and PIMs templates. However, the question is - does the template affect the properties of the synthesized materials?

In this study, we focused on representatives of two classes of polymers such as BCPs and PIMs that were reported to have a different mechanism of interaction with gas-phase metal oxide precursors [9,21,31] to investigate the effect of the polymer template in the synthesis of highly porous ZnO nanostructures. ZnO nanostructures and conformal coating represent an important class of materials with great potential in optoelectronics, photocatalysis, gas sensing, biochemical sensing, and fabrication of antibacterial coating [36–41]. However, the existing traditional methods are limited in the degree of the structure, composition, and porosity control. Since ZnO porous structures can be obtained by infiltration of the polymer template with metal precursors from the gas and solution phases, we also investigated how the infiltration technique affects the synthesized materials. This study provides insight into the relationship between the preparation techniques, the structure, and the properties of nanoporous ZnO coatings. Since ZnO is one of the most exploited metal oxides in gas sensing, we used the sensitivity of ZnO to ethanol vapors to characterize the performance of ZnO synthesized using BCP (PS-P4VP(25-25)) and PIM (PIM-1) templates and two different infiltration techniques with gas phase and solution-based precursors.

2. Experimental procedure

2.1. Sample preparation

The ZnO coatings were prepared by adopting two infiltration techniques: solution-based infiltration (SBI) and swelling-assisted sequential infiltration synthesis (SIS). The polymer of intrinsic microporosity (PIM-1) was synthesized using previously reported procedures [42]. The block copolymer poly(styrene-*block*-4-vinylpyridine) (PS-P4VP) (specifically in this study (PS(25)-PVP(25))) was purchased from Polymer Source, Inc.

The PIM-1 was dissolved in chloroform to prepare a solution of 0.03 g/mL concentration. PIM-1 templates on QCM substrates with titanium-coated electrodes and SiO_2/Si substrates were prepared by spin coating the polymers at 800 rpm for 40 s. After spin coating, the samples were baked at 70 °C for 1 h for full evaporation of the chloroform and improved adhesion of the film to the substrates. The thickness of the resulting coatings calculated from the QCM analysis and confirmed by the ellipsometry was ~200 nm.

The PS-P4VP BCP was dissolved in chloroform to prepare a solution of 2 wt%. The BCP samples were spin-coated on the silicon wafer and QCMs at 2000 rpm for 40 s.

The samples for the X-ray diffraction (XRD) study were prepared using a paper filter (Whatman, Grade I) as a substrate for the polymer template during the swelling and infiltration steps [43]. Paper filters were immersed in the polymer solution and sonicated for 30 mins for absorption of the polymers inside the cellulose matrix.

2.1.1. Infiltration of the polymer templates with solution-phase precursors

ZnO samples were synthesized by the immersion of the PIM-1 and PS-P4VP(25-25) templates in a solution of zinc acetylacetonate, Zn $(acac)_2$ in ethanol at different concentrations (from 0.05 wt% up to 1 wt % concentration) at 75 °C for 1 h. The ethanol solution of $Zn(acac)_2$ was stirred for 1 h for complete solubility of the $Zn(acac)_2$ powder in ethanol and left for a few hours before immersion of the polymer. The temperature of this procedure was selected based on the earlier results indicating the higher swelling rates of the polymer at an elevated temperature [18].

2.1.2. Infiltration of the polymer templates with gas-phase precursors

Infiltration of the polymer templates with gas-phase precursors (diethyl zinc (DEZ) and water vapors) was conducted using the SIS technique which is a variant of the ALD process for vapor phase infiltration of ZnO in the polymer template [23]. Before the infiltration, the PS-P4VP films were swollen to increase the efficiency of the infiltration of the PS-P4VP template with zinc oxide precursors [18]. The swelling was performed in ethanol at 75 °C for 1 h, followed by drying under the fume hood for 2–3 h to prevent collapsing of the swelling-induced free volume in the polymers. PIM films deposited on the substrates were immersed in ethanol heated to 75 °C for ~1 h and then dried out at nitrogen flow to remove the residue of the solvent. Such treatment was reported to increase the free volume in the polymer template [44] and increase gas permeability [45] that was attributed to improved efficiency of the PIM-1 infiltration with the gas phase precursors [32].

The SIS was done using Veeco Savannah S100 ALD System. Several deposition runs were made to optimize the recipe for infiltration of ZnO by using diethyl zinc precursor (DEZ). The samples were placed in the reactor chamber at 90 °C, below the glass transition temperature of the PS-P4VP to avoid compromising the integrity of the polymer structure. Nitrogen (20 sccm) was introduced into the reactor chamber prior to the infiltration. The polymer templates were exposed to 5 cycles of DEZ precursor for 400 s, when the infiltration of the polymer was completed, the excess of the reactant was evacuated and followed by exposure to 5 cycles of H_2O for 200 s, the chamber was then purged with 100 sccm of nitrogen to remove excess byproducts.

2.2. Polymer removal

UV ozone cleaner (UVOCSR16x16 OES, 254 nm UV wavelength) was used for the removal of polymer templates on the QCM crystal after the infiltration. The samples were exposed to UV ozone treatment for 10 h at room temperature. For the Si/SiO_2 samples, the polymer templates were removed in a Thermo Scientific Lindberg Blue M Furnace for 4 h at 450 °C with Oxygen flowing through the furnace tube, to transport polymer particles removed away from the surface of the sample.

2.3. QCM Analysis and gas sensing measurement

The QCM analysis was used for the in situ quantitative analysis of the swelling events, infiltration process after the SBI and SIS, and in situ analysis of infiltration during the sensing measurements. The QCM is made of an AT-cut piezoelectric quartz crystal (1 in. in diameter) which oscillates in a shear mode with a resonant frequency of 5 MHz. The Titanium and gold-coated QCMs were purchased from Fil-Tech. The changes in the resonant frequency of the QCM oscillations when in contact with a liquid media and mass were observed with the SRS QCM200 controller.

Gas sensing test was performed in a custom-built vacuum chamber connected to a nitrogen gas, and ethanol supply. In the chamber, two samples, one deposited on the QCM and one deposited on the Si/SiO_2 substrate prepared with the SIS and SBI preparation procedure, were placed next to each other to simultaneously measure ethanol adsorption efficiency and the induced changes in electrical conductivity. A custom-designed stainless-steel holder was used to hold the QCM sample in place for the controlled temperature tests. QCM samples were used for the sensing assessment as they accommodate nanometer scale coatings and can detect changes resulting from even submonolayer coverage of the adsorbed species. In comparison, standard Brunauer–Emmett–Teller (BET) measurements require much larger, at least a couple of grams,

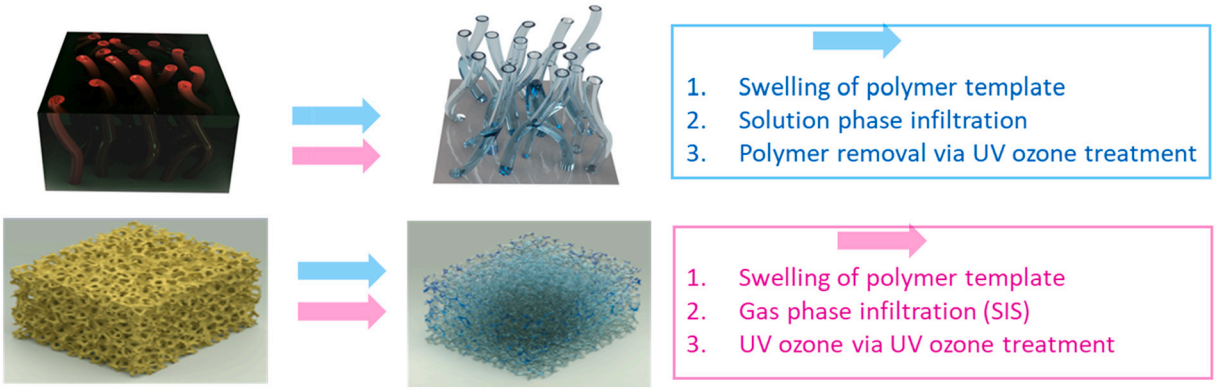

Fig. 1. Depiction of the polymer templates and the approaches used in the synthesis of porous ZnO structures.

mass of material. Electrical measurements were conducted using the van der Pauw method with four probes connected to the corners of the sample and the resistance was measured with a 2401 Keithley Source Meter. To eliminate the effect of air and disruptive moisture on the ZnO samples, the chamber was pumped down to ~10^{-3} Torr after placing the QCM and silicon dioxide samples in the vacuum chamber. The samples were then exposed to the ethanol vapors introduced to the chamber, and the pressure was monitored using a 275 Granville-Phillips Vacuum Gauge. The resonant frequency of the QCM and the resistance readings on the source meter were allowed to stabilize at room temperature before readings were recorded.

The adsorption capacity of the QCM samples was estimated from the change in the QCM resonant frequency that is directly proportional to the added mass [46,47]:

$$\Delta f = -\frac{2f^2}{A\sqrt{\rho_q \mu_q}}\Delta m \quad (1)$$

where f is the frequency of oscillation of the unloaded crystal, ρ_q is the density of quartz (2.648 g cm^{-3}), μ_q is the shear modulus of quartz (2.947×10^{11} g cm^{-1} S^{-2}), A is the QCM surface area, and Δm is the mass change.

Five different tests were carried out on each sample upon exposure to ethanol vapor and venting of the chamber.

2.4. Characterization

Scanning Electron Microscopy (SEM) analysis of the samples was

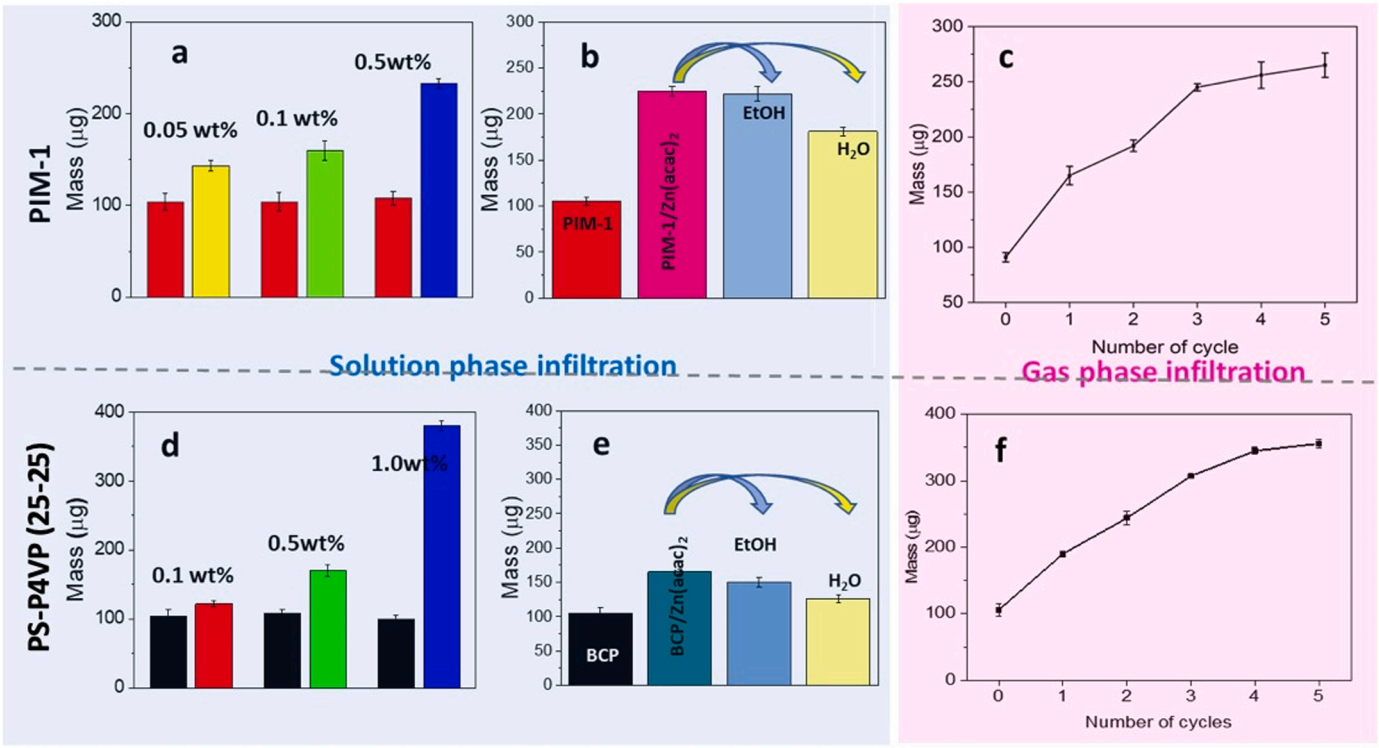

Fig. 2. Summary of mass changes of the polymer templates as a result of their infiltration with zinc oxide precursors measured by the QCM. Mass increase caused by the infiltration of PIM-1 and PS-P4VP templates (a and d, respectively) (the masses of PIM-1 and PS-P4VP deposited for each experiment shown in a and d are depicted as red and black bars, correspondingly) using solution-phase precursor with different concentrations of $Zn(acac)_2$ in ethanol (the concentration used in the experiments are denoted on the figures); (b and e) evolution of the mass of PIM-1 and PS-P4VP templates infiltrated with 0.5 wt% of $Zn(acac)_2$ upon their exposures to EtOH and H_2O; (c) evolution of the mass of PIM-1 and PS-P4VP templates as a result of 1–5 SIS cycles (the polymer templates were treated with EtOH prior SIS as described in the Experimental Details).

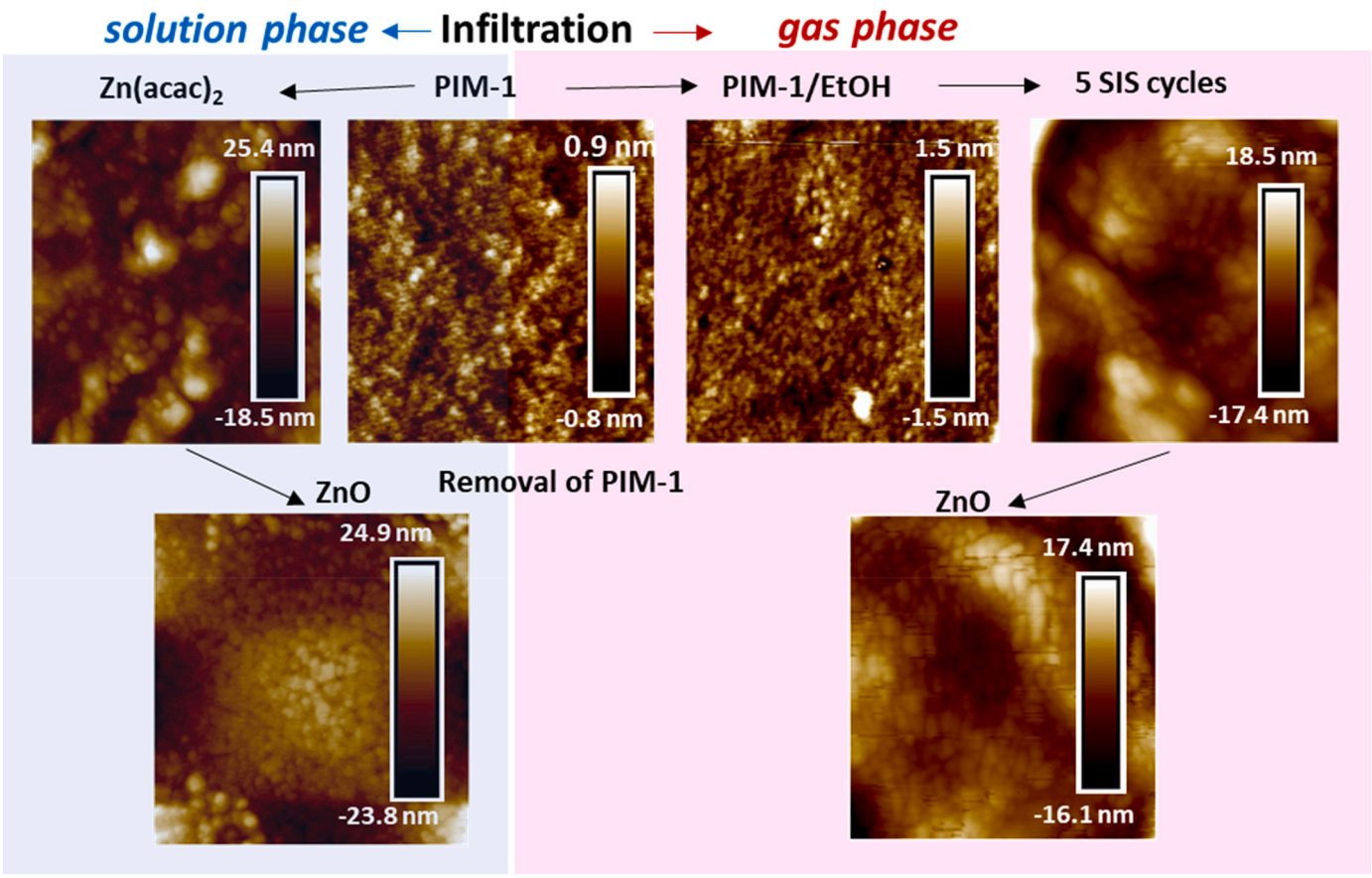

Fig. 3. AFM surface topography images of initial PIM-1 and PIM-1 templates underwent infiltration with zinc oxide precursors from solution and gas phases followed by polymer removal resulting in the formation of porous ZnO coatings. The AFM scan size is 140 nm.

performed using an FEI Nova SEM. The analysis of the surface topography and roughness profile of the samples was performed with a Bruker Multimode Atomic Force Microscopy (AFM). The images were acquired in tapping mode in the air with a scan rate of 0.5 Hz using Antimony doped Silicon tips with a spring constant of 42 N/m. X-Ray Diffraction (XRD) analysis was done with Bruker D2 Phaser and Bruker D8 Discover. Contact angle measurements were conducted by the Sessile water drop (10 μL) method using a Ramé-Hart 250 contact angle goniometer. X-ray photoelectron spectroscopy (XPS) measurements were done with a PHI 5000 Versaprobe spectrometer with monochromatic 1486.6 eV Al Kα radiation. All binding energies were corrected for the charge shift using the C 1s peak at 284.5 eV, and the energy resolution was 0.1 eV.

3. Results and discussion

Previously, we have demonstrated that porous ZnO conformal coatings can be synthesized using BCPs by SIS using a gas-phase precursor [23]. In this study we explore a new type of polymer template such as the PIM-1 template for the fabrication of porous coatings. Also, we examined if polymer templates can be infiltrated with metal oxide precursors from the solution phase that can simplify the synthesis of porous metal oxide coatings. Fig. 1 summarizes the templates and infiltration techniques used in this study to synthesize porous ZnO. The scoring of the properties was done using the performance of ZnO porous structures for ethanol sensing.

While methanol is the most frequently used solvent to treat PIM-1 [44,45] to improve its gas permeability, here we tested other solvents to systematically investigate the effect of solvent treatment on the subsequent infiltration of PIM-1 with gas phase precursors. We used the QCM technique to monitor the in-situ change in resonant frequency between bare QCM crystals and the polymer-coated QCM crystals before and after their exposure to different media. While PIM-1 is soluble only in tetrahydrofuran (THF) and chloroform, our data indicated a very small decrease in polymer mass after treatment with other solvents such as methanol, ethanol, acetone, and toluene (Fig. S1). It can be attributed to the removal of the chloroform trapped during spin-PIM-1 coating and/or removal of oligomers possibly present in the initial PIM-1. Our QCM results suggest that there is no significant change in the mass of the polymer after swelling in ethanol and methanol, which indicates that no molecular degradation of the polymer occurred during swelling and all changes shown in the QCM experiment can be attributed to its volumetric expansion (Fig. S1a). We choose ethanol for all experiments with PIM-1 since the ethanol is used to swell BCPs and the use of the same solvent enables minimizing of the synthesis parameters. Therefore, we used ethanol as a treatment solvent to prepare both PS-P4VP and PIM-1 templates for gas-phase infiltration and as a solvent of zinc acetylacetonate ($Zn(acac)_2$) that served as a solution-phase precursor. Similar to methanol, exposure of PIM-1 to ethanol was found to be very effective in preserving the porosities created in the polymer due to the high vapor pressure of ethanol, thereby preventing the mobility of the polymer chains toward equilibrium packing [48].

After ethanol treatment, PS-P4VP and PIM-1 templates were exposed to gas or solution phase precursors. QCM technique was used to analyze the efficiency of the infiltration by monitoring the mass change of the samples (Fig. 2). In the case of gas-phase precursors (Fig. 2c), a significant mass gain was observed when 3 ALD cycles were performed. After 3 cycles, the mass gain significantly slows down indicating that PIM-1 is approaching full infiltration. Therefore, we limited the number of ALD cycles in SIS to 5.

We have tested different concentrations of $Zn(acac)_2$ in ethanol to

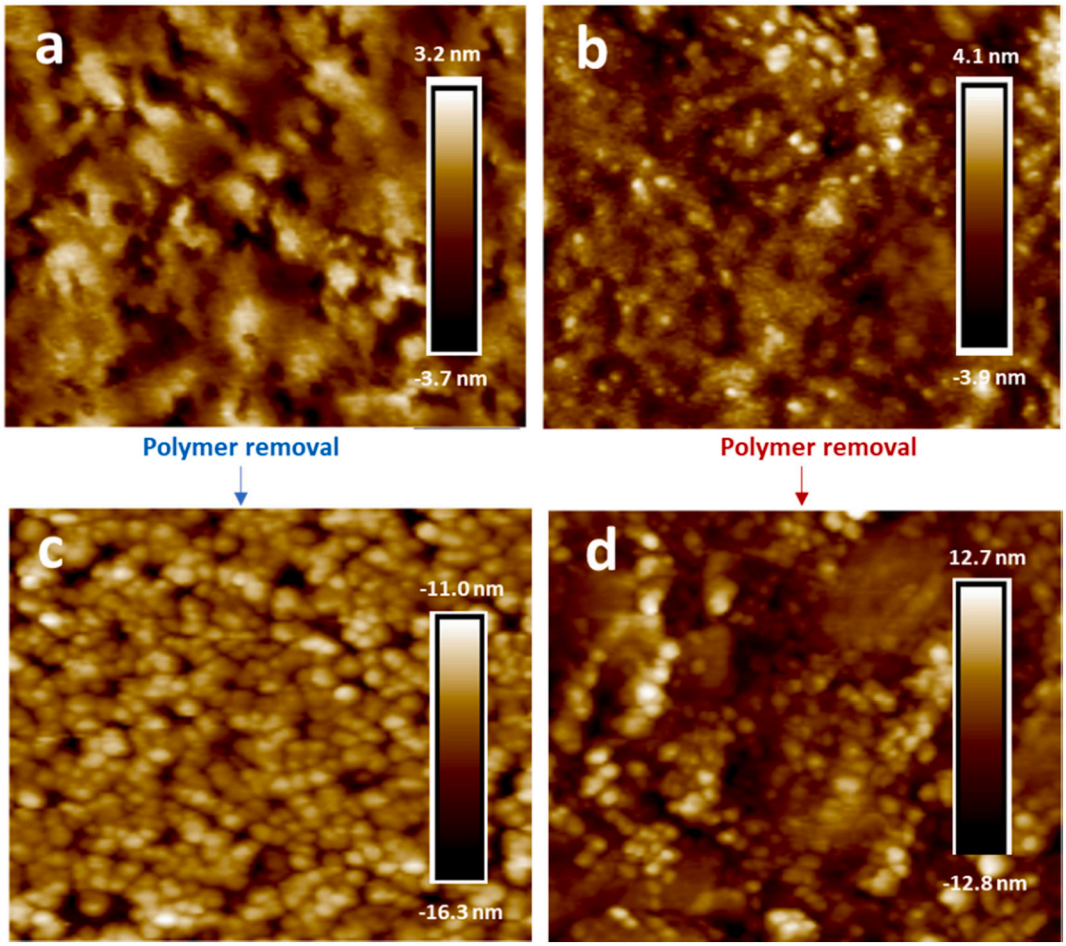

Fig. 4. AFM surface topography images of BCP (PS-b-P4VP(25-25)) templates infiltrated using solution (1 wt% of $Zn(acac)_2$ in EtOH) and gas-phase precursors (a and b, respectively) and AFM surface topography images of porous ZnO coatings formed as a result of polymer removal of PS-P4VP templates infiltrated using solution and gas-phase precursors (c and d, respectively). The AFM scan size is 140 nm.

infiltrate PIM-1 with zinc precursors from the solution phase. An increase in the samples' mass upon their exposure to a more concentrated $Zn(acac)_2$ ethanol solution indicates that PIM-1 efficiently adsorbs the zinc precursor dissolved in ethanol (Fig. 2a). The substantial rise in the mass of the PIM-1 immersed into $Zn(acac)_2$ ethanol solutions with concentrations above 0.1 wt% we attribute to the possible crystallization of zinc precursors from the solution.

QCM study indicated that $Zn(acac)_2$ adsorbed by polymer did not desorb back into ethanol as evidenced by no mass change upon immersion of the infiltrated polymer templates into ethanol. However, exposure of infiltrated polymers with $Zn(acac)_2$ to water was associated with a loss of ~half mass gained during the infiltration step (Fig. 2b, e). It can indicate the desorption of $Zn(acac)_2$; however, it has a lower solubility in water as compared to ethanol. Therefore, no change in mass upon immersion of infiltrated polymer in ethanol and mass decrease observed in water point out to a reaction between the infiltrated Zn $(acac)_2$ and water (e.g., exchange of acetylacetonate ligand with OH group). Fig. 3 shows that almost no changes were observed in the surface topography of the swelled PIM (Fig. 3b), in comparison to the initial PIM (Fig. 3a). This further confirms the stability of the polymer after swelling in ethanol. However, the swelled polymer exhibits an increase in roughness height, indicating the presence of swelling-induced porosities. Surface topography for the PS-P4VP(25-25) and PIM infiltrated with zinc oxide precursors from solution and gas phases, and all-inorganic ZnO films formed after polymer removal are shown in Figs. 3 and 4.

After infiltration of the polymer templates with zinc oxide precursors from solution and gas-phase precursors, the polymer templates were removed via UV ozone cleaning [49] that resulted in the formation of nanoporous ZnO films. The AFM images indicate the smooth and uniform nature of these nanoporous films for both polymer templates and both infiltration approaches with the resulting nanoporous structure being highly dependent on the template type. The films prepared using the solution-phase infiltration demonstrate a little higher degree of the refinement in comparison to the vapor-phase infiltration which is attributed to the salt agglomeration effect upon the polymer removal process. As a result, the solution-phase processed coatings are expected to exhibit larger accessibility of the surfaces to the environment.

The SEM images (Fig. 5) further confirm that zinc oxide films obtained with the same type of polymer template demonstrate similar morphologies regardless of the type of the zinc oxide precursor they were synthesized with. The SEM analysis shows that the surface of ZnO films obtained with PIM-1 templates is characterized by the presence of some circular features. Their formation we attribute to the capturing of the gas or solvent molecules by PIM-1 during its spin-coating that are released during polymer removal causing the appearance of circular dimples [32].

Fig. 5e demonstrates the X-ray diffraction (XRD) patterns of the porous ZnO samples prepared using two types of polymer templates with both solution and gas-phase precursors. The diffraction peaks of the synthesized ZnO films were indexed to the hexagonal wurtzite crystal structure of ZnO. As it is evidenced by rather narrow XRD peaks, ZnO samples prepared using solution-phase precursors are highly crystalline. However, the XRD spectra of ZnO samples prepared using gas-phase

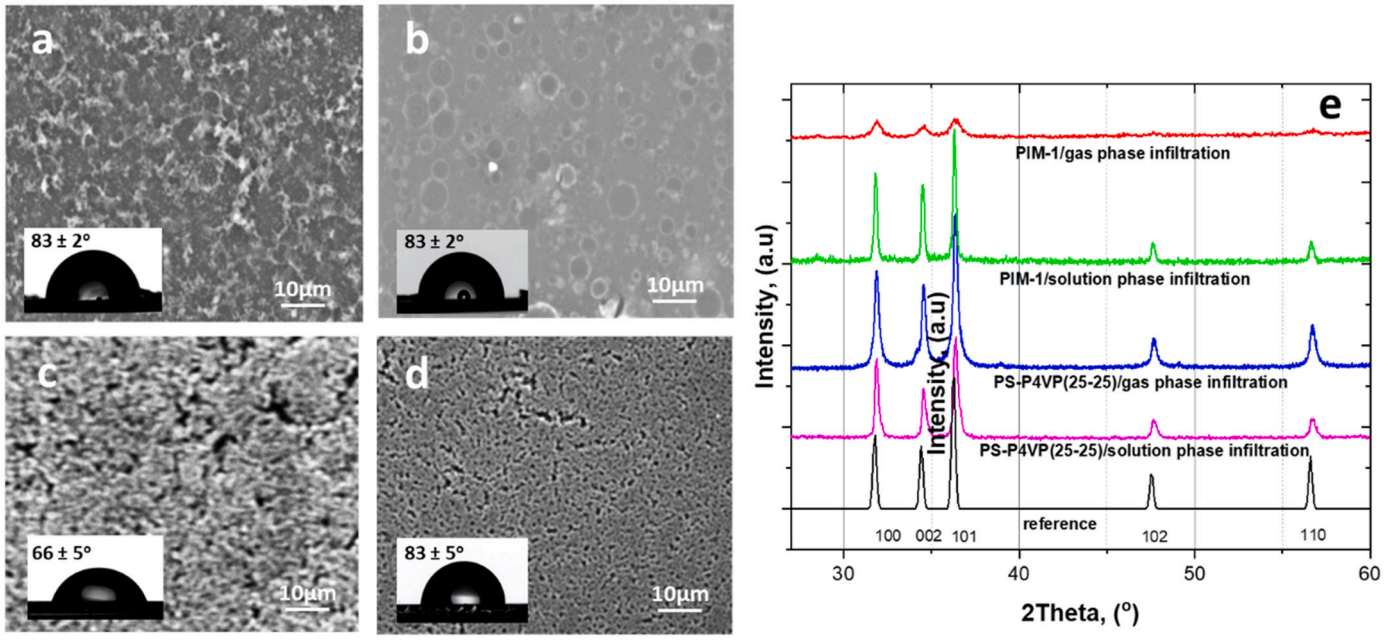

Fig. 5. SEM images of porous ZnO coatings obtained using PIM-1 templates with solution and gas-phase precursors, (a and b, respectively), and using BCP (PS-b-P4VP(25-25)) templates with solution and gas precursors (c and d, respectively). 0.5 w t% and 1 wt% concentrations of $Zn(acac)_2$ in EtOH were used for PIM-1 and PS-b-P4VP(25-25) templates, respectively. 5 cycles of SIS were used for the infiltration of polymer templates with gas-phase precursors. The insets demonstrate the data of the contact angle measurements on the corresponding surfaces. (e) XRD spectra of porous ZnO film synthesized by infiltration of PIM-1 and PS-b-P4VP(25-25) templates using the solution and gas-phase precursors.

precursors are characterized by broader peaks indicating the nanocrystalline nature of the synthesized material. A comparison of their XRD spectra indicates that the PIM-1 template enables the synthesis of ZnO with a smaller crystalline size. These results are in agreement with the highly nanocrystalline structure of ZnO nanowires synthesized via the infiltration of lithographically patterned SU-8 polymer template using gas-phase precursors [28].

XRD spectra demonstrate strong diffraction peaks for all studied samples. These peaks can be indexed to the hexagonal structure with space group symmetry $P6_3mc$ of the ZnO wurtzite phase, which is in a good agreement with data reported for ZnO wurzite phase (Fig. 5e) [50]. The slight shift of 2Theta to higher values can be indicative to less than 0.5 % lattice strain (Fig. 5e).

We conducted XPS studies to analyze the surface composition of synthesized porous ZnO films. High-resolution XPS spectra of the Zn $2p_{3/2}$ and O 1s regions are shown in Fig. 6. For all samples, the Zn $2p_{3/2}$ peak was fitted to only one Gaussian. The XPS spectra of all porous ZnO films have Zn $2p_{3/2}$ peaks at ~1021.2 eV, suggesting a +2 oxidation state of surface zinc [51] and that the surface of samples is Zn dominated since the stoichiometric ZnO reveals a corresponding peak at 1022 eV [52]. The most intense peaks of the XPS spectra in O 1s regions of ZnO samples obtained with gas-phase precursors are at ~529.8 eV that correspond to the Zn—O bond in ZnO lattice [52–53]; however, these peaks are shifted to slightly lower values of binding energies when gas-phase precursors were used to infiltrate both PIM-1 and PS-P4VP templates. Since all binding energies were corrected for the charge shift using the C 1s peak, we can exclude the charging effect and attribute such shifts to the subtle difference in atomic arrangement around oxygen atoms in ZnO samples prepared with gas-phase precursors. The XPS spectra of ZnO synthesized with PS-P4VP(25-25) could be deconvoluted into two Gaussian sub-peaks, at ~530 eV and 531.5 eV, that is characteristic of oxygen vacancies [52,53]. The broader and more asymmetric peaks of the O 1s peaks indicate that ZnO obtained using PIM-1 templates has more species at the surface. We deconvoluted corresponding spectra into three different Gaussian peaks. ZnO obtained using PIM-1 and gas-phase precursors also revealed a peak at 531.5 eV indicative of oxygen vacancies and a peak at ~533 eV that is often attributed to -OH [52–53]. ZnO samples synthesized using PIM-1 and solution phase precursors revealed a peak at 533 eV and at ~532 eV that can be attributed to either chemically adsorbed O_2 [52,53] or it can a result of the shift of the peak corresponding to oxygen vacancies due to similar origin as the shift of the most intense peak. On the other hand, previously, the peak at 532.6 eV was attributed to loosely bound oxygen on the surface due to H_2O or OH groups bonded to metal [53].

ZnO is a commonly used intrinsic n-type semiconductor material with a bandgap of 3.37 eV, for the detection of various gas molecules due to its low cost and non-toxicity in nature [54,55]. When ZnO is exposed to an ambient atmosphere, oxygen molecules are adsorbed on the surface of ZnO and then ionize into oxygen species by capturing electrons from the conduction band, leading to the creation of a surface depletion layer, band bending in the direction of reducing electrons, increase in the potential barrier and thus increasing the sensor resistance. Upon exposure of the ZnO surface to a reductive gas such as ethanol, the oxygen species will react with these ethanol gas molecules, leading to the formation of gaseous CO_2 and H_2O. Trapped electrons are released back to the conduction band, band bending is reduced, depletion width and the potential barrier for electron transport decreases, resulting in a decrease in the sensor resistance [36,55–57]. Typically elevated temperatures (350 °C) are required to achieve a reduction in resistance [58]. Previously, we have shown that nanoporous ZnO enabled significantly higher sensitivity at much lower temperatures (down to room temperature) [23]. Therefore, we have tested the resistivity change in response to ethanol vapors at room temperature.

The gas sensing tests for our synthesized porous ZnO films were conducted in a custom-made vacuum chamber. The chamber is equipped with a 4-point probe and a QCM to simultaneously measure the change in electrical resistance and change in QCM resonant frequency during exposure to ethanol. The resonant frequency shift is directly proportional to the mass of ethanol adsorbed [59]. Changes in the electrical conductivity and QCM frequency of the prepared ZnO films were also analyzed. Comparison of the resistance change and mass change can help to estimate the surface accessibility and sensitivity of

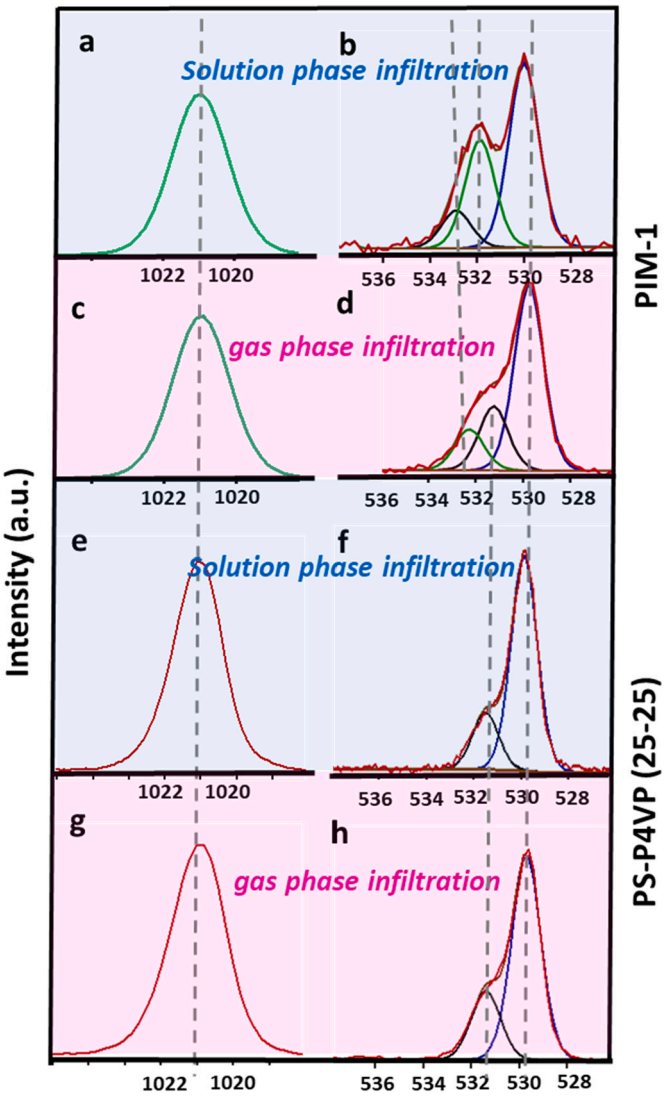

Fig. 6. XPS spectra of Zn $2p_{3/2}$ and O 1s peaks for porous ZnO coatings synthesized with PIM-1 and PS-P4VP(25-25).

the synthesized porous ZnO coatings.

For consistency in comparison, we've chosen the samples synthesized with 5 cycles of SIS and adjusted the concentrations of $Zn(acac)_2$ in ethanol to provide adsorption of similar concentrations of zinc oxide precursors. Thus, we used 0.5 wt% and 1 wt% concentrations of $Zn(acac)_2$ for PIM-1 and PS-P4VP(25-25), respectively. Note, that 5 cycle of SIS results in the infiltration of different amount of zinc oxide precursors into PIM-1 and PS-P4VP templates (Fig. 2). Therefore, Fig. 7 demonstratethe sensing performance of the samples synthesized with the amount of ZnO equivalent to the amount of ZnO obtained via 5 cycles of SIS for each type of polymer; However, we also normalized the mass change and resistivity responses of ZnO samples obtained with PS-P4VP (Fig. 7, data shown by dotted curves) to directly compare the performance of ZnO synthesized with different templates. The summary of the sensing results for the SBI-prepared ZnO films compared to the SIS at room temperature is shown in Fig. 7. The pressure increase in the pressure-time graph depicts the inflow of ethanol into the chamber. The pressure drop is indicative of ethanol evacuation from the chamber. All ZnO sensors demonstrated an increase in mass and decrease in resistance. The ZnO samples synthesized with PS-P4VP(25-25) demonstrated a more than two times higher mass increase upon their exposure to the ethanol vapors as compared to ZnO synthesized with PIM-1. ZnO films obtained by infiltration of PIM-1 with gas-phase precursors revealed the worst performance, while infiltration of PIM-1 using solution-phase resulted in similar resistivity change to ZnO samples obtained using solution-phase infiltration of PS-P4VP(25-25) that demonstrated ~2.5 higher change in mass measured in QCM experiments (Fig. 7). This points out that ZnO synthesized with solution-phase precursor using PS-P4VP has more surface accessible for ethanol molecules; however, the surface of ZnO film obtained using PIM-1 and solution phase precursor is better suited for decomposition ethanol.

Table 1 summarizes the resulting ethanol surface area coverage of 200 nm thick ZnO films. To analyze the availability of the surfaces to the ethanol adsorption, we extract the surface coverage values from the measured changes in the QCM resonant frequency. For this, we can assume that ethanol molecules attach to the ZnO surface vertically. Therefore, the ethanol coverage A_E in a simple model can be evaluated as:

$$A_E = N \times \pi r^2 \tag{2}$$

with N defining the number of the adsorbed on the nanoporous ZnO films ethanol molecules extracted from the detected changes in the adsorbed mass as:

$$N = \frac{\Delta m \times N_A}{M_{ethanol}} \tag{3}$$

By combining Eqs. (2) and (3) we roughly estimate the availability of the ZnO surface for the ethanol coverage as:

$$A_E = \frac{\Delta m N_A \pi r^2}{M_{ethanol}} \tag{4}$$

Note, that both higher performing ZnO samples are highly crystalline, while samples with lower crystallinity demonstrated lower performance. In fact, samples with the smaller size of the crystallites reveal the worst results in terms of their resistivity change upon their exposure to ethanol. Therefore, we conclude that higher crystallinity of ZnO is associated with more robust and pronounced resistivity change. Smaller mass change of ZnO obtained with PS-P4VP(25-25) and gas-phase precursor as compared to ZnO synthesized using the same polymer template but with solution-phase precursors indicates that the presence of Zn $(acac)_2$ in ethanol can also affect the swelling of BCP and can favor more complete micelle opening in spin-coated BCP [49] resulting in the synthesis of ZnO with a more accessible surface.

4. Conclusion

In conclusion, we have investigated the effect of the structure and composition of the polymer template on the synthesis of the porous conformal inorganic coatings. Using the synthesis of ZnO as a model system, we have compared two types of polymers, PIM-1 and PS-P4VP (25-25), that have a different mechanism of interactions with metal oxide precursors. We have also demonstrated that the infiltration of polymer templates can be efficiently achieved using both gas phase and solution phase precursors. We showed that the crystallinity of the synthesized ZnO is mainly affected by the state of the precursor (gas or solution phase) and does not depend on the polymer template type. Thus, we demonstrated that infiltration of polymer templates using solution-phase precursors (e.g. $Zn(acac)_2$) enabled higher crystallinity as compared to samples obtained using gas-phase precursors (so-called SIS or VPI). The concentration of the metal salt in the solution can be matched to achieve the amount of metal oxide comparable with the amount synthesized via SIS or VPI. All synthesized samples revealed the promising potential for sensing at room temperature. Interestingly, more crystalline ZnO conformal films synthesized with solution-phase precursors demonstrated better performance in ethanol sensing tests as compared to samples synthesized with gas-phase precursors. We also showed that the surface of porous ZnO synthesized with BCP (here PS-

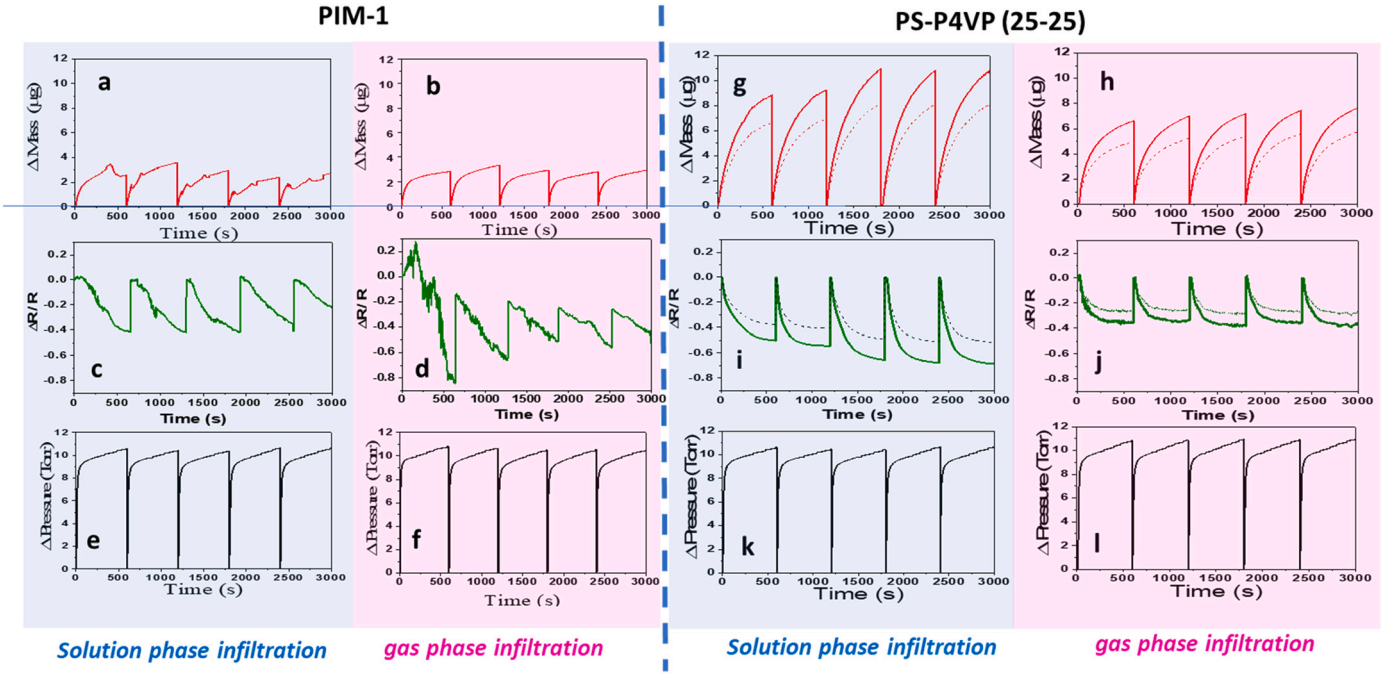

Fig. 7. Summary of change in mass and resistance upon the exposure of porous ZnO synthesized using different polymer templates and precursors to ethanol vapor at room temperature. (a-d) and (g-j) correspond to ZnO samples synthesized using PIM-1 and PS-P4VP, respectively. The pressure profiles for each experiment are shown in e, f, k, and l. Dotted curves in g-j represent the signal change characteristic to the same amount of ZnO as in a-d.

Table 1
Summary of the ethanol surface area coverage of the films revealed by the QC measurements.

	PIM-1		PS-P4VP (25-25)	
	Solution-phase	Gas-phase	Solution-phase	Gas-phase
Surface coverage	302 cm^2	278 cm^2	794 cm^2	596 cm^2

P4VP) is more accessible than the surface of ZnO synthesized with PIM. However, despite the lower surface accessibility for ethanol molecules, ZnO synthesized via infiltration of PIM-1 with solution-phase precursors demonstrates the largest change in resistivity upon its exposure to ethanol vapor. Therefore, we conclude that solution and gas-phase infiltrations are promising approaches for the synthesis of uniform metal oxide or mixed metal oxide porous conformal coatings The surface of the synthesized metal oxide can depend on the type of the polymer template that, in turn, can affect their properties (e.g. biofilm growth, catalytic, etc.). Our results open the access to the synthesis of conformal metal oxide where gas-phase precursors are not available, or gas phase precursors can be available at high temperatures at which polymer template undergoes glass phase transition or deteriorates.

Supplementary data to this article can be found online at https://doi.org/10.1016/j.surfcoat.2022.129107.

CRediT authorship contribution statement

Khalil Omotosho: Investigation, Data Curation, Writing. John Tran: Data Curation. Elena Shevchenko: Supervision, Investigation, Writing. Diana Berman: Supervision, Investigation, Conceptualization, Writing.

Declaration of competing interest

The authors declare that they have no known competing financial interests or personal relationships that could have appeared to influence the work reported in this paper.

Data availability

Data will be made available on request.

Acknowledgments

The authors acknowledge the support of this work by the National Science Foundation, Award No. 2045662. This work was performed in part at the University of North Texas' Materials Research Facility. Work at the Center for Nanoscale Materials was supported by the U.S. Department of Energy, Office of Science, Office of Basic Energy Sciences, under Contract No. DE-AC0206CH-11357.

References

[1] Y.-C. Tseng, Q. Peng, L.E. Ocola, D.A. Czaplewski, J.W. Elam, S.B. Darling, Etch properties of resists modified by sequential infiltration synthesis, J. Vac. Sci. Technol., B: Nanotechnol. Microelectron.: Mater., Process., Meas., Phenom. 29 (6) (2011), 06FG01.
[2] S.I. Stupp, P.V. Braun, Molecular manipulation of microstructures: biomaterials, ceramics, and semiconductors, Science 277 (5330) (1997) 1242–1248.
[3] G.M. Whitesides, J.P. Mathias, C.T. Seto, Molecular self-assembly and nanochemistry: a chemical strategy for the synthesis of nanostructures, Science 254 (5036) (1991) 1312–1319.
[4] S.-M. Lee, E. Pippel, U. Gösele, C. Dresbach, Y. Qin, C.V. Chandran, T. Bräuniger, G. Hause, M. Knez, Greatly increased toughness of infiltrated spider silk, Science 324 (5926) (2009) 488–492.
[5] S. Mann, G.A. Ozin, Synthesis of inorganic materials with complex form, Nature 382 (6589) (1996) 313–318.
[6] K.E. Gregorczyk, D.F. Pickup, M.G. Sanz, I.A. Irakulis, C. Rogero, M. Knez, Tuning the tensile strength of cellulose through vapor-phase metalation, Chem. Mater. 27 (1) (2014) 181–188.
[7] S.-M. Lee, E. Pippel, O. Moutanabbir, J.-H. Kim, H.-J. Lee, M. Knez, In situ Raman spectroscopic study of al-infiltrated spider dragline silk under tensile deformation, ACS Appl. Mater. Interfaces 6 (19) (2014) 16827–16834.
[8] E. Barry, A.U. Mane, J.A. Libera, J.W. Elam, S.B. Darling, Advanced oil sorbents using sequential infiltration synthesis, J. Mater. Chem. A 5 (6) (2017) 2929–2935.
[9] D. Berman, E. Shevchenko, Design of functional composite and all-inorganic nanostructured materials via infiltration of polymer templates with inorganic precursors, J. Mater. Chem. C 8 (2020) 10604–10627.
[10] M.A. Saccone, R.A. Gallivan, K. Narita, D.W. Yee, J.R. Greer, Additive manufacturing of micro-architected metals via hydrogel infusion, Nature (2022) 1–2.

[11] C.Z. Leng, M.D. Losego, Vapor phase infiltration (VPI) for transforming polymers into organic–inorganic hybrid materials: a critical review of current progress and future challenges, Mater.Horiz. 4 (5) (2017) 747–771.
[12] Y. She, E. Goodman, J. Lee, B.T. Diroll, M. Cargnello, E.V. Shevchenko, D. Berman, Block-copolymer assisted synthesis of all inorganic highly porous heterostructures with highly accessible thermally stable functional centers, ACS Appl. Mater. Interfaces 11 (33) (2019) 30154–30162.
[13] R.Z. Waldman, D.J. Mandia, A. Yanguas-Gil, A.B. Martinson, J.W. Elam, S. B. Darling, The chemical physics of sequential infiltration synthesis—a thermodynamic and kinetic perspective, J. Chem. Phys. 151 (19) (2019), 190901.
[14] C. Sanchez, P. Belleville, M. Popall, L. Nicole, Applications of advanced hybrid organic–inorganic nanomaterials: from laboratory to market, Chem. Soc. Rev. 40 (2) (2011) 696–753.
[15] R. Clay, R. Cohen, Synthesis of metal nanoclusters within microphase-separated diblock copolymers: a 'universal'approach, Supramol. Sci. 2 (3–4) (1995) 183–191.
[16] J. Ciebien, R. Clay, B. Sohn, R. Cohen, Brief review of metal nanoclusters in block copolymer films, New J. Chem. 22 (7) (1998) 685–691.
[17] H. Al Kutubi, L. Rassaei, W. Olthuis, G. Nelson, J. Foord, P. Holdway, M. Carta, R. Malpass-Evans, N. McKeown, S. Tsang, Polymers of intrinsic microporosity as high temperature templates for the formation of nanofibrous oxides, RSC Adv. 5 (89) (2015) 73323–73326.
[18] D. Berman, S. Guha, B. Lee, J.W. Elam, S.B. Darling, E.V. Shevchenko, Sequential infiltration synthesis for the design of low refractive index surface coatings with controllable thickness, ACS Nano 11 (3) (2017) 2521–2530.
[19] D.H. Yi, C.-Y. Nam, G. Doerk, C.T. Black, R.B. Grubbs, Infiltration synthesis of diverse metal oxide nanostructures from epoxidized diene-styrene block copolymer templates, ACS Appl.Polym.Mater. 1 (4) (2019) 672–683.
[20] R.Z. Waldman, D.J. Mandia, A. Yanguas-Gil, A.B.F. Martinson, J.W. Elam, S. B. Darling, The chemical physics of sequential infiltration synthesis—a thermodynamic and kinetic perspective 151(19), 2019.
[21] M.D. Losego, Q. Peng, Atomic layer deposition and vapor phase infiltration, in: Surface Modification of Polymers, 2019, pp. 135–159.
[22] E.K. McGuinness, F. Zhang, Y. Ma, R.P. Lively, M.D. Losego, Vapor phase infiltration of metal oxides into nanoporous polymers for organic solvent separation membranes, Chem. Mater. 31 (15) (2019) 5509–5518.
[23] D. Pleshek, J. Tran, Y. Li, A. Shirani, E.V. Shevchenko, D. Berman, Swelling-assisted sequential infiltration synthesis of nanoporous ZnO films with highly accessible pores and their sensing potential for ethanol, ACS Appl. Mater. Interfaces 13 (30) (2021) 35941–35948.
[24] Y. She, J. Lee, B.T. Diroll, T.W. Scharf, E.V. Shevchenko, D. Berman, Accessibility of the pores in highly porous alumina films synthesized via sequential infiltration synthesis, Nanotechnology 29 (49) (2018), 495703.
[25] J. Lee, V. Hasannaeimi, T.W. Scharf, D. Berman, Mechanical and chemical robustness of the aluminum oxide-infiltrated block copolymer films and the resulting aluminum oxide coatings, Surf. Coat. Technol. 399 (2020), 126204.
[26] Q. Peng, Y.C. Tseng, S.B. Darling, J.W. Elam, Nanoscopic patterned materials with tunable dimensions via atomic layer deposition on block copolymers, Adv. Mater. 22 (45) (2010) 5129–5133.
[27] C.T. Black, R. Ruiz, G. Breyta, J.Y. Cheng, M.E. Colburn, K.W. Guarini, H.-C. Kim, Y. Zhang, Polymer self assembly in semiconductor microelectronics, IBM J. Res. Dev. 51 (5) (2007) 605–633.
[28] C.-Y. Nam, A. Stein, K. Kisslinger, C.T. Black, Electrical and structural properties of ZnO synthesized via infiltration of lithographically defined polymer templates, Appl. Phys. Lett. 107 (20) (2015), 203106.
[29] L.E. Ocola, Y. Wang, R. Divan, J. Chen, Multifunctional UV and gas sensors based on vertically nanostructured zinc oxide: volume versus surface effect, Sensors 19 (9) (2019) 2061.
[30] M. Biswas, J.A. Libera, S.B. Darling, J.W. Elam, New insight into the mechanism of sequential infiltration synthesis from infrared spectroscopy, Chem. Mater. 26 (21) (2014) 6135–6141.
[31] F. Zhang, E.K. McGuinness, Y. Ma, Y. Ren, J.E. Leisen, M.D. Losego, R.P. Lively, Vapor-phase-infiltrated AlOx/PIM-1 "Hybrid Scaffolds" as solution-processable amine supports for CO2 adsorption, ACS Appl.Polym.Mater. 3 (9) (2021) 4460–4469.
[32] C. Ji, Z. Zhang, K. Omotosho, D. Berman, B. Lee, R. Divan, S. Guha, E. Shevchenko, Porous but mechanically robust all inorganic antireflective coatings synthesized using polymers of intrinsic microporosity, ACS Nano 16 (9) (2022) 14754–14764.
[33] E.C. Dandley, C.D. Needham, P.S. Williams, A.H. Brozena, C.J. Oldham, G. N. Parsons, Temperature-dependent reaction between trimethylaluminum and poly (methyl methacrylate) during sequential vapor infiltration: experimental and ab initio analysis, J. Mater. Chem. C 2 (44) (2014) 9416–9424.
[34] S. Wang, K. Shi, A. Tripathi, U. Chakraborty, G.N. Parsons, S.A. Khan, Designing intrinsically microporous polymer (pim-1) microfibers with tunable morphology and porosity via controlling solvent/nonsolvent/polymer interactions, ACS Appl. Polym.Mater. 2 (6) (2020) 2434–2443.
[35] W. Ogieglo, B. Ghanem, X. Ma, I. Pinnau, M. Wessling, How much do ultrathin polymers with intrinsic microporosity swell in liquids? J. Phys. Chem. B 120 (39) (2016) 10403–10410.
[36] V.S. Bhati, M. Hojamberdiev, M. Kumar, Enhanced sensing performance of ZnO nanostructures-based gas sensors: a review, Energy Rep. 6 (2020) 46–62.
[37] N.P. Shetti, S.D. Bukkitgar, K.R. Reddy, C.V. Reddy, T.M. Aminabhavi, ZnO-based nanostructured electrodes for electrochemical sensors and biosensors in biomedical applications, Biosens. Bioelectron. 141 (2019), 111417.
[38] M.A. Borysiewicz, ZnO as a functional material, a review, Crystals 9 (10) (2019) 505.
[39] Y. Zhang, T.R. Nayak, H. Hong, W. Cai, Biomedical applications of zinc oxide nanomaterials, Curr. Mol. Med. 13 (10) (2013) 1633–1645.
[40] C. Klingshirn, ZnO: material, physics and applications, ChemPhysChem 8 (6) (2007) 782–803.
[41] L. Guo, Y. Wang, Y. Shang, X. Yang, S. Zhang, G. Wang, Y. Wang, B. Zhang, Z. Zhang, Preparation of Pd/PdO@ZnO-ZnO nanorods by using metal organic framework templated catalysts for selective detection of triethylamine, Sensors Actuators B Chem. 350 (2022), 130840.
[42] N. Du, G.P. Robertson, J. Song, I. Pinnau, S. Thomas, M.D. Guiver, Polymers of intrinsic microporosity containing trifluoromethyl and phenylsulfone groups as materials for membrane gas separation, Macromolecules 41 (24) (2008) 9656–9662.
[43] Y. She, E.D. Goodman, J. Lee, B.T. Diroll, M. Cargnello, E.V. Shevchenko, D. Berman, Block-co-polymer-assisted synthesis of all inorganic highly porous heterostructures with highly accessible thermally stable functional centers, ACS Appl. Mater. Interfaces 11 (33) (2019) 30154–30162.
[44] M.L. Jue, C.S. McKay, B.A. McCool, M.G. Finn, R.P. Lively, Effect of nonsolvent treatments on the microstructure of PIM-1, Macromolecules 48 (16) (2015) 5780–5790.
[45] C.R. Mason, L. Maynard-Atem, K.W.J. Heard, B. Satilmis, P.M. Budd, K. Friess, M. Lanč, P. Bernardo, G. Clarizia, J.C. Jansen, Enhancement of CO2 affinity in a polymer of intrinsic microporosity by amine modification, Macromolecules 47 (3) (2014) 1021–1029.
[46] D. Berman, J. Krim, Impact of oxygen and argon plasma exposure on the roughness of gold film surfaces, Thin Solid Films 520 (19) (2012) 6201–6206.
[47] G. Sauerbrey, Verwendung von Schwingquarzen zur Wägung dünner Schichten und zur Mikrowägung, Z. Phys. 155 (2) (1959) 206–222.
[48] M.L. Jue, C.S. McKay, B.A. McCool, M. Finn, R.P. Lively, Effect of nonsolvent treatments on the microstructure of PIM-1, Macromolecules 48 (16) (2015) 5780–5790.
[49] Y. She, J. Lee, B.T. Diroll, B. Lee, S. Aouadi, E.V. Shevchenko, D. Berman, Rapid synthesis of nanoporous conformal coatings via plasma-enhanced sequential infiltration of a polymer template, ACS Omega 2 (11) (2017) 7812–7819.
[50] A. Šarić, M. Vrankić, D. Lützenkirchen-Hecht, I. Despotović, Ž. Petrović, G. Dražić, F. Eckelt, Insight into the growth mechanism and photocatalytic behavior of tubular hierarchical ZnO structures: an integrated experimental and theoretical approach, Inorg. Chem. 61 (6) (2022) 2962–2979.
[51] R. Al-Gaashani, S. Radiman, A.R. Daud, N. Tabet, Y. Al-Douri, XPS and optical studies of different morphologies of ZnO nanostructures prepared by microwave methods, Ceram. Int. 39 (3) (2013) 2283–2292.
[52] F.-M. Chang, S. Brahma, J.-H. Huang, Z.-Z. Wu, K.-Y. Lo, Strong correlation between optical properties and mechanism in deficiency of normalized self-assembly ZnO nanorods, Sci. Rep. 9 (1) (2019) 905.
[53] S. Gandla, S.R. Gollu, R. Sharma, V. Sarangi, D. Gupta, Dual role of boron in improving electrical performance and device stability of low temperature solution processed ZnO thin film transistors, Appl. Phys. Lett. 107 (15) (2015), 152102.
[54] J. Cui, L. Shi, T. Xie, D. Wang, Y. Lin, UV-light illumination room temperature HCHO gas-sensing mechanism of ZnO with different nanostructures, Sensors Actuators B Chem. 227 (2016) 220–226.
[55] L. Zhu, W. Zeng, Room-temperature gas sensing of ZnO-based gas sensor: a review, Sensors Actuators A Phys. 267 (2017) 242–261.
[56] Z.U. Abideen, J.-H. Kim, A. Mirzaei, H.W. Kim, S.S. Kim, Sensing behavior to ppm-level gases and synergistic sensing mechanism in metal-functionalized rGO-loaded ZnO nanofibers, Sensors Actuators B Chem. 255 (2018) 1884–1896.
[57] J.-H. Kim, J.-H. Lee, Y. Park, J.-Y. Kim, A. Mirzaei, H.W. Kim, S.S. Kim, Toluene- and benzene-selective gas sensors based on Pt-and Pd-functionalized ZnO nanowires in self-heating mode, Sensors Actuators B Chem. 294 (2019) 78–88.
[58] T.T. Suzuki, T. Ohgaki, Y. Adachi, I. Sakaguchi, M. Nakamura, H. Ohashi, A. Aimi, K. Fujimoto, Ethanol gas sensing by a Zn-terminated ZnO(0001) bulk single-crystalline substrate, ACS Omega 5 (33) (2020) 21104–21112.
[59] J. Xie, H. Wang, M. Duan, QCM chemical sensor based on ZnO colloid spheres for the alcohols, Sensors Actuators B Chem. 203 (2014) 239–244.